Available online at www.sciencedirect.com
SCIENCE DIRECT®
Journal of Nuclear Materials 324 (2004) 41–51
journal of nuclear materials
www.elsevier.com/locate/jnucmat

Simulations of low energy cascades in fcc Pu metal at 300 K and constant volume

Steven M. Valone *, Michael I. Baskes, Marius Stan, Terence E. Mitchell, Andrew C. Lawson, Kurt E. Sickafus

Materials Science and Technology Division, Structure-Property Relations Group, Los Alamos National Laboratory, Los Alamos, NM 87545, USA

Received 22 April 2003; accepted 12 September 2003

Abstract

Recently progress has been achieved with a modified embedded atom method (MEAM) potential for pure Pu. The MEAM potential is able to capture the most salient features of atomic volume and enthalpy of solid and liquid Pu metal as a function of temperature at zero pressure. The atomic volume difference between monoclinic (α-phase) and fcc (δ-phase) was captured nearly quantitatively. From molecular dynamics (MD) simulations, we find that Pu, under these conditions, has an approximately 10 eV minimum displacement threshold energy, very low compared to most other fcc metals, and shows less crystallographic anisotropy in this minimum. At 0 K, the constant volume cell relaxes to a rhombohedrally distorted structure, which is connected to the low minimum displacement threshold energy. Split interstitials orient themselves in a ⟨1 0 0⟩ direction and migrate over a 0.056 eV barrier. Mono-vacancies migrate over a 0.84–1.00 eV barrier.

1. Introduction

One approach to modeling radiation damage accumulation in a material starts with the number of point defects produced by the individual radiative cascades. These point defects, consisting of vacancies and interstitials, are then allowed to migrate. Vacancies and interstitials annihilate each other when they react, but can accumulate into larger scale clusters when they encounter other vacancies and interstitials, respectively. The vacancies and interstitials migrate at different rates and hence tend to separate over time, leaving a population of 'freely migrating defects' consisting of a distribution of interstitial and vacancy cluster sizes. Other models not discussed here use the population of freely migrating defects as input to follow the gradual accumulation process that produces extended defects, such as dislocations, stacking faults and bubbles. The extended defects are ultimately responsible for the structural and mechanical changes to an irradiated material that we refer to as damage.

Atomistic cascade simulations of radiative processes are now routinely used as a means of determining the initial creation of point defects in a crystalline material and the very early stages of vacancy-interstitial recombination, immediately after a radiative event. The point-defect production rates for many fcc metals and for some bcc metals have been determined through such simulations. In all cases to date, the pristine lattices were the thermodynamic ground-states of their respective materials and always the highest density phase at ambient conditions.

Plutonium (Pu) metal is different. The metal is typically formed in the fcc phase, which is the lowest density phase at ambient pressure, by addition of phase-stabilizing alloying. The thermodynamically stable phase of Pu metal is monoclinic, which is 25% higher in density.

* Corresponding author. Tel.: +1-505 667 2067; fax: +1-505 667 8021.
E-mail address: smv@lanl.gov (S.M. Valone).

0022-3115/$ - see front matter © 2003 Elsevier B.V. All rights reserved.
doi:10.1016/j.jnucmat.2003.09.006

As a consequence, a central issue in self-irradiation damage accumulation in Pu metal is how the defect accumulation process normal for fcc metals plays out against the thermodynamic proximity of a higher density, more stable phase. Performing cascade simulations capable of correctly predicting the structure and mobility of the resulting point defects is predicated on the availability of a potential energy surface that correctly captures at least these essential features of the phase diagram of the material.

Consequently, modeling thermodynamics and defect production in plutonium metal itself, to say nothing of Pu alloys, has proven to be singularly difficult. Recently, however, progress has been achieved in the form of a modified embedded atom method (MEAM) [1,2] potential for pure Pu [3]. The MEAM potential is able to capture the most salient features of atomic volume and enthalpy of solid and liquid Pu metal as a function of temperature at zero pressure (p) (Fig. 1(a) and (b)). Most significantly the atomic volume difference between the monoclinic (α) and fcc (δ) phases is captured nearly quantitatively.

Here we use this potential to explore the formation of point defects due to self-irradiation in Pu metal at room temperature (RT) and constant volume (V). We find that our model of fcc Pu metal under constant T and constant V conditions has a very low minimum displacement threshold energy compared to most other fcc materials, has narrower spread in the minimum displacement threshold energy as a function of crystallographic direction of the cascade, and, at low projectile energies, yields markedly greater damage than is predicted by the Kinchin–Pease (KP) or Norgett–Robinson–Torrens (NRT) models of damage accumulation [4–6]. The damage levels reported here are based on relatively short annealing times.

For δ-Pu to be stable at RT, it is alloyed with suitable elements such as gallium (Ga) or aluminum. Since an atomistic description of any Pu alloy is beyond the scope of this work, we have attempted to model defect formation in the Ga-stabilized alloy using a model of Pu metal. Neither the real metal nor the MEAM model of Pu metal is stable as an fcc lattice at STP. During our analysis, we have found it sufficient to use constant V instead of constant p conditions. Constant V conditions have stabilized lattices of over 30 000 atoms at cascade energies up to 300 eV. Comparison between defect formation at 600 K and constant average p ($p = 0$ Pa) versus 600 K and constant V, where the fcc lattice is stable under both conditions, showed good agreement. The volumes for the constant-V simulations were those of the lattices equilibrated at 600 K and 0 Pa. Since our intent was to simulate the self-irradiation damage behavior of Ga-stabilized Pu alloys via the pure Pu metal, and the linear thermal expansion coefficient of the alloy is small, not less than -9×10^{-6}/K at 810 K [7–9] and

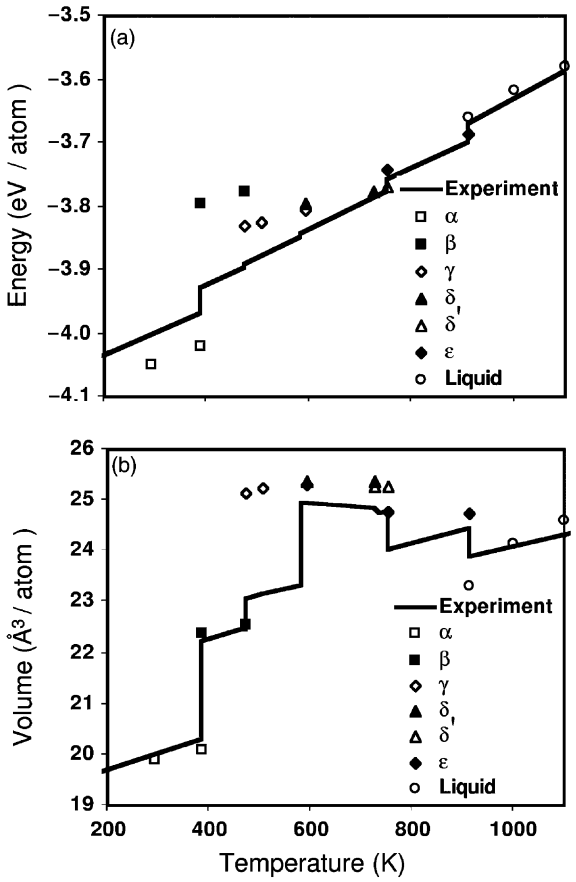

Fig. 1. Comparison of the calculated and experimental energy (a) and volume (b) per atom of the equilibrium plutonium phases as a function of temperature, for Pu metal as modeled by the MEAM potential described in Section 2 with parameters reported in Table 1 [3]. The energies are relative to isolated, noninteracting atoms at infinity. The data are shown over the experimental regions of stability at 0 Pa. The monoclinic angles for the α and the β phases were held fixed at the experimental values. The differences in enthalpy and volume between the α and δ phases closely approximate the experimental values.

decreasing with temperature, the approximately 0.3% linear changes (in the physical system) on cooling to 300 K were deemed negligible. We took this as reasonable assurance that our choice of boundary conditions has not unduly skewed our simulation results.

Some of the peculiarities of the δ-Pu lattice predicted by our MEAM potential are illustrated in Fig. 2(a)–(c). The lattice undergoes a rhombohedral distortion along the body diagonal of a doubly-redundant cubic cell. Each unit cell contains 8 atoms. Viewed along a principle fcc axis the Pu atoms form a dimerized structure. The crystal structure shown in Fig. 2(a) is achieved by quenching at constant V to 0 K a structure which had been annealed at 600 K, where the δ-Pu lattice is stable

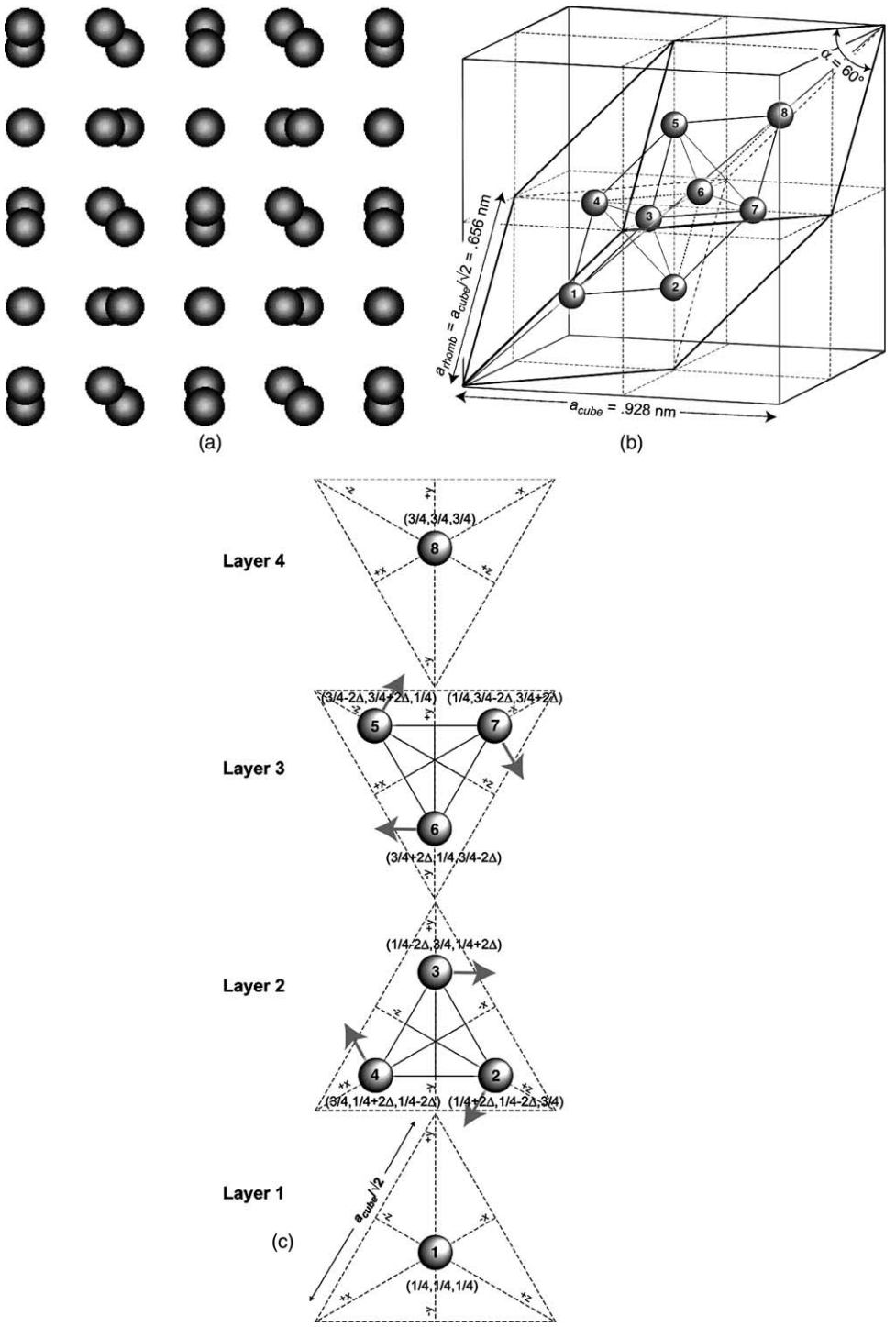

Fig. 2. (a) Constant V, 0 K structure of MEAM Pu metal lattice with rhombohedral distortions. (b) Atom positions within the rhombohedral unit cell with edges equal to $a_{\mathrm{cube}}/\sqrt{2} = 0.6562$ nm. The center line denotes the body diagonal of the cubic cell. (c) Layer stacking schematic diagram for atom positions in the rhombohedral unit cell shown in (a). Layers occur sequentially from bottom to top along the body diagonal of the doubly-redundant cubic unit cell. The 8 atoms in the unit cell are found at fractional heights 3/12, 5/12, 7/12, and 9/12, relative to the length of the cubic body diagonal, i.e., $\sqrt{3}a_{\mathrm{cube}}$.

at 0 Pa. The distortion may arise from the proximity in energy of the α-Pu structure, even though the simulated structure is quite dissimilar to the α structure. The MEAM potential, being a single, adiabatic surface, must capture both the fcc and monoclinic structures as local minima. It is significant that the distortions stay at about the same level, 0.025 nm, even at 0 K. Again, we emphasize that imposing symmetric, constant-V boundary condition imparts metastability to the fcc structure down to 0 K.

The following Section summarizes the MEAM potential development for Pu. In Section 3, we describe the structure and diffraction predictions for the distorted δ-Pu phase. In Section 4.1, the conditions and results of the cascade simulations are described. In Section 4.2, the conditions and results for estimating the migration rates of the split interstitials and mono-vacancies are described. Finally the most pertinent results and their significance are summarized.

2. Modified embedded atom method (MEAM) potential for Pu

In the embedded atom method (EAM), the total cohesive energy is expressed as the sum of contributions from each atom in the system. For a system consisting of a single type of atom, that sum over all atoms in the system has the form

$$E = \sum_i \left(F(\bar{\rho}_i) + \frac{1}{2} \sum_{j \neq i} \phi(R_{ij}) \right), \tag{1}$$

where F is the embedding function, whose argument is the background density, $\bar{\rho}_i$, at atomic site i, and ϕ is a pair potential with separation R_{ij} between atoms i and j. In EAM $\bar{\rho}_i$ has been approximated as spherically-averaged densities.

The MEAM potential is an extension of EAM in which an angular dependence is allowed in the background density. For bcc and hcp metals and covalent materials, this difference between MEAM and EAM has proven to be crucial. The most prevalent functional form for the background density in the MEAM formalism consists of

$$\bar{\rho} = \rho^{(0)}(1 + \Gamma)^{1/2}, \tag{2}$$

where $\bar{\rho}$ is the background electron-density at a chosen atom in the lattice and $\rho^{(0)}$ is the sum of the spherically-averaged electron-densities of the neighboring atoms for the chosen atom. The angular modification is constructed from the sum

$$\Gamma = \sum_{l=1}^{3} t^{(l)} (\rho^{(l)}/\rho^{(0)})^2. \tag{3}$$

The coefficients $t^{(l)}$ are constants, the partial electron-densities, $\rho^{(l)}$, are linear combinations of exponentially-decaying functions of the atomic separations, and the coefficients of the linear combination are components of unit vectors between the chosen atom and its neighbors. This functional form is effectively a local Legendre polynomial expansion of the total background density about each atomic site [2,3].

Four other points are also worth noting. (1) The embedding function, F, was represented by the bond-order-motivated form

$$F(\bar{\rho}) = AE_c(\bar{\rho}/\rho_0)\ln(\bar{\rho}/\rho_0), \tag{4}$$

where E_c is the cohesive energy and ρ_0 is the background electron density at equilibrium. (2) The pair potential, ϕ, was determined from the difference between the cold-curve, E^u, and F for a reference configuration of the system. (3) The cold-curve was assumed to have the form

$$E^u = -E_c(1 + a^* + \alpha\delta(a^*)^3/(a^* + \alpha))\exp(-a^*), \tag{5}$$

with

$$a^* = \alpha(R/r_e - 1) \tag{6}$$

and

$$\alpha^2 = (9\Omega B)/E_c. \tag{7}$$

The variables r_e, Ω, and B are the nearest-neighbor distance, atomic volume, and bulk modulus, respectively, all evaluated at equilibrium in the reference structure (fcc here). (4) The cubic term in a^* is a small correction with strength δ, which was found to be important for Pu. This term is directly related to the pressure derivative of the bulk modulus. The interested reader is directed to Refs. [1,2], and references therein, for further details on the meaning of the specific concepts employed in the MEAM potential.

The MEAM potential parameter values are given in Table 1. The values used to fit the potential are noted. Fig. 1(a) and (b) show how the MEAM-Pu potential tracks the major trends in the enthalpy of formation and atomic volumes as a function of temperature. The most difficult phases to represent were γ (distorted diamond), for enthalpy, and β (34 atoms/cell monoclinic), for atomic volume. Nevertheless, the differences in atomic volume between the α- and δ-phases are very close to the best-available experimental values. These energetic and volumetric differences were seen as critical for self-irradiation damage simulations because of the possibility of radiation-induced phase transformation of the metastable δ-phase. Because there are several phases of significantly lower atomic volume, transformation into one or more of these would counteract the normal radiation-induced swelling tendencies of fcc metals [4].

Table 1
Sources and values of MEAM parameters for plutonium

Parameter	Source	Value
E_c (eV)	Cohesive energy of liquid Pu[a]	3.8
r_e (nm)	Nearest neighbor distance in δ-Pu[a]	0.328
α (dimensionless)	Bulk modulus of Ga-stabilized δ-Pu[b] (30 GPa)	3.31
A (dimensionless)	Relative enthalpy of δ-Pu and ε-Pu[a] (0.11 eV)	1.05
$\beta^{(0)}$ (dimensionless)	Shear modulus of Ga-stabilized δ-Pu[b] (16 GPa)	2.39
$\beta^{(1)}$ (dimensionless)	Nominal value	1.0
$\beta^{(2)}$ (dimensionless)	Nominal value	6.0
$\beta^{(3)}$ (dimensionless)	Volume per atom of δ-Pu[a] 25.0 Å^3	9.0
$t^{(1)}$ (dimensionless)	Nominal value	1.0
$t^{(2)}$ (dimensionless)	Shear modulus of Ga-stabilized δ-Pu[b] (4.8 GPa)	4.64
$t^{(3)}$ (dimensionless)	Relative enthalpy of δ-Pu and α-Pu[a] (0.503 eV)	−0.8
Δ (dimensionless)	Pressure derivative of bulk modulus of δ-Pu[c] (11)	0.46

Where appropriate experimental data was not available, nominal values were chosen that are similar to the values used for other elements.
[a] Ref. [10].
[b] Ref. [11].
[c] Ref. [12].

3. Crystal structure of distorted δ-Pu

Based on the coordinates of the δ-Pu structure at constant V and quenched to 0 K, the distortions from the ideal fcc positions could be determined by inspecting the arrangement of atoms in a 64 atom simulation cell. The determination will be an aid to present and future spectroscopic studies of Pu metal and alloys as they age. In the following, we will show that this model results in a rhombohedral distortion of the δ-Pu structure and we will present a calculated X-ray powder diffraction pattern to illustrate the large deviations of the simulated structure from fcc.

3.1. The ideal (undistorted) δ-Pu structure based on an fcc unit cell

Ideal δ-Pu is an isometric phase with a lattice parameter given by $a = 0.464$ nm. The Bravais lattice is face-centered cubic (fcc); the space group is No. 225 ($Fm\bar{3}m$ or $F\frac{4}{m}\bar{3}\frac{2}{m}$). The structure can be derived by placing a Pu atom on a 4a Wyckoff equipoint at the unit cell origin (fractional cell coordinates (x, y, z) given by (0, 0, 0)). Lattice translations given by (0,0,0; $0, \frac{1}{2}, \frac{1}{2}$; $\frac{1}{2}, 0, \frac{1}{2}$; $\frac{1}{2}, \frac{1}{2}, 0$), which define equivalent positions, then generate the four atoms per unit cell.

3.2. The structure of distorted δ-Pu based on a rhombohedral unit cell

The distorted δ-Pu phase can be described using a rhombohedral unit cell with lattice parameter given by $a = 0.6562$ nm. and rhombohedral angle $\alpha = 60°$. No deviation from $\alpha = 60°$ was permitted in the simulation cell. The unit cell contains 8 atoms. Fig. 2 shows the positions for Pu atoms in the rhombohedral unit cell before the atoms undergo their rhombohedral distortion from cubic symmetry (i.e., the atoms are shown in their ideal, 'fcc' positions). The symmetry for the distorted structure can be represented in space group (S.G.) No. 167 ($R\bar{3}c$ or $R\bar{3}2/c$). The rhombohedral cell is related to a cubic unit cell that itself is doubly-redundant compared to the ideal fcc unit cell. The ideal fcc unit cell is defined by lattice parameter $a_{fcc} = 0.464$ nm. Consequently, the doubly-redundant cube has cell length $a_{cube} = 2a_{fcc} = 0.928$ nm, and the rhombohedral unit cell along the cube body diagonal has cell length $a_{rhomb} = a_{cube}/\sqrt{2} = 0.6562$ nm.

Two Pu atoms occupy equipoint 2a (point symmetry 32) in S.G. $R\bar{3}c$, with fractional coordinates $\{\frac{1}{4}, \frac{1}{4}, \frac{1}{4}\}$ and $\{\frac{3}{4}, \frac{3}{4}, \frac{3}{4}\}$. The 2a atom positions are not dependent on atomic relaxations. Six Pu atoms occupy equipoint 6e (point symmetry 2). This equipoint is defined by a single positional parameter, x, given by $x = \frac{3}{4} - 2\Delta$. The fractional coordinates of the 6e atoms are $\{\frac{3}{4} - 2\Delta, \frac{3}{4} + 2\Delta, \frac{1}{4}\}$, $\{\frac{3}{4} + 2\Delta, \frac{1}{4}, \frac{3}{4} - 2\Delta\}$, $\{\frac{1}{4}, \frac{3}{4} - 2\Delta, \frac{3}{4} + 2\Delta\}$, $\{\frac{1}{4} + 2\Delta, \frac{1}{4} - 2\Delta, \frac{3}{4}\}$, $\{\frac{1}{4} - 2\Delta, \frac{3}{4}, \frac{1}{4} + 2\Delta\}$, and $\{\frac{3}{4}, \frac{1}{4} + 2\Delta, \frac{1}{4} - 2\Delta\}$. Dilation Δ is equivalent to the ratio of the relaxed displacement of the Pu atoms, to the length of the doubly-redundant cubic unit cell ($a_{cube} = 0.928$ nm). Based on the MEAM model for the δ-Pu structure, $\Delta = 0.026$ nm$/0.928$ nm $= 0.028$. This parameter represents the dilation from the ideal fcc structure of δ-Pu (for $\Delta = 0$, the δ-Pu adopts the unit cell described in 3.1). Upon dilation, when viewed along a principle fcc axis, the Pu atoms form a dimerized structure. The dilation parameter Δ was used in structure factor calculations for the volume-stabilized lattice.

Fig. 2(c) shows a layer stacking schematic diagram for atom positions in the rhombohedral unit cell. Layers

occur sequentially from bottom to top along the body diagonal of the doubly-redundant cubic unit cell. The 8 atoms in the unit cell are found at fractional heights 3/12, 5/12, 7/12, and 9/12, relative to the length of the cubic body diagonal, i.e., $\sqrt{3}a_{\text{cube}}$. The atom labels 1–8 correspond to the atom labels in Fig. 2(b). Also shown in Fig. 2(c) are projections of equilateral triangles associated with the termination of the $\pm\boldsymbol{x}$, $\pm\boldsymbol{y}$, and $\pm\boldsymbol{z}$ axes of the rhombohedral unit cell. These triangles (shown dotted) occur at heights 1/3 and 2/3 relative to the cube body diagonal, length $\sqrt{3}a_{\text{cube}}$. The edges of these equilateral triangles are defined by lengths $a_{\text{cube}}/\sqrt{2}$. Projections of the $\boldsymbol{x}$, $\boldsymbol{y}$, and $\boldsymbol{z}$ axes for the rhombohedral unit cell are also shown, with $\pm\boldsymbol{x}$ etc., labeled for each coordinate. The solid triangles in Layers 2 and 3 represent equilateral triangles associated with the termination of the $\pm\boldsymbol{x}$, $\pm\boldsymbol{y}$, and $\pm\boldsymbol{z}$ axes of the small rhombohedral cell inscribed by the 8 atoms when located in their ideal positions (Fig. 2). The edges of these triangles are defined by lengths $a_{\text{cube}}/2\sqrt{2} = 0.328$ nm, which is the nearest neighbor spacing of atoms in ideal 'fcc' δ-Pu. The sense of the dilations due to Δ are indicated by grey arrows. All dilations are in planes perpendicular to the cube body diagonal. Fractional coordinates for each atom are indicated on the diagram.

The distorted crystal structure for δ-Pu, as predicted by MEAM and described above, is achieved by quenching to 0 K a structure which had been annealed at 600 K, where the δ-Pu lattice is stable at 0 Pa. This distortion may be arising from the proximity in energy of the α-Pu structure. In the MEAM model for Pu, both the α and the δ phases must be described by a single potential energy surface. The process of fitting both phases may be introducing the distortion by producing a spurious local minimum, or the distortion may be a real physical effect from the mixture of the two states. Again, we emphasize that imposing symmetric, constant-V boundary condition imparts metastability to the fcc structure down to 0 K. At temperatures above about 100 K, thermal averaging is expected to render the distorted and ideal structures indistinguishable with respect to most characterization techniques.

3.3. Predicted diffraction patterns

The predicted X-ray powder diffraction patterns for conventional δ-Pu versus the rhombohedrally distorted δ-Pu structure described above are shown in Fig. 3(a) and (b), respectively. The X-ray diffraction pattern simulations are based on X-ray diffraction using CuKα radiation ($\lambda = 0.1542$ nm).

As with all fcc Bravais lattices, the structure factor corresponding to the powder pattern shown in Fig. 3(a), is defined by a set of allowed reflections for which Miller indices are restricted by the following conditions for $hkl : h + k, k + l, (l + h) = 2n$. In the case of diffraction

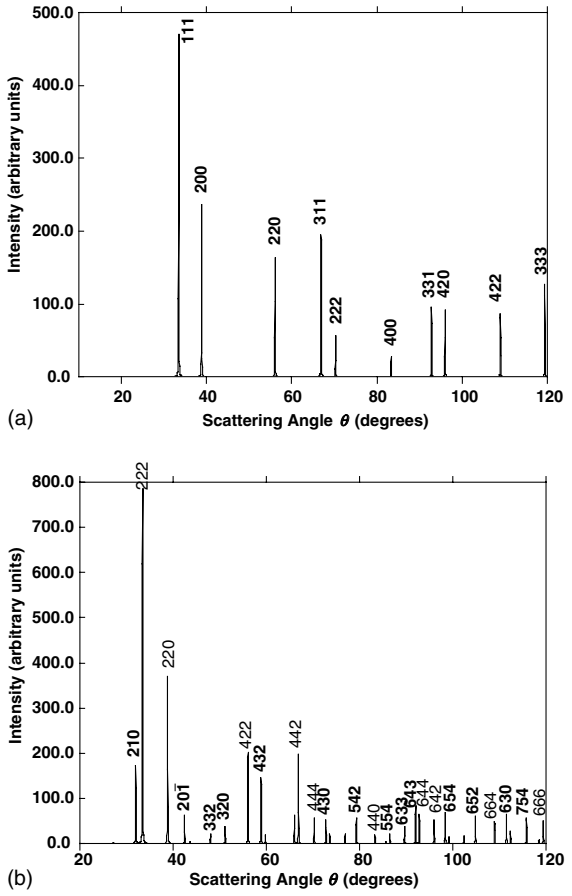

Fig. 3. (a) Simulated powder X-ray diffraction pattern from ideal (undistorted) fcc δ-Pu ($\lambda = 0.1542$ nm). (b) Simulated powder X-ray diffraction pattern from distorted δ-Pu ($\lambda = 0.1542$ nm).

from the new, rhombohedrally distorted δ-Pu crystal structure (Fig. 3(b)), the structure factor consists of one condition limiting possible reflections: $hhl : l = 2n$. This condition defining allowed reflections arises from the presence of c-glide planes in the structure. It should be noted that this condition is sign-sensitive. This means that reflections given by $h\bar{h}l$, l odd are allowed, not forbidden reflections. The net effect of the atomic displacements associated with the distorted δ-Pu phase, is to produce many weak or medium intensity reflections (labeled in bold in Fig. 3(b)), in addition to the primary 'fcc' reflections.

This rhombohedrally distorted structure has not been observed in any X-ray, neutron, or electron diffraction experiment that we are aware of. The rhombohedral structure may be sensitive to the formation of anti-phase domains that would broaden the superlattice reflections to invisibility if the domains were small enough. Such domains were not observed in the simulation, however.

Also, the rhombohedral distortion is almost certainly temperature dependent. Warming the MD cell to just 100 K is enough to make the lattice appear to be fcc on any thermally averaged basis.

4. Simulations of defect production in a cascade

4.1. Simulation technique

Simulations of defect production were carried out by selecting one atom in the simulation cell to act as the primary knock-on atom (PKA). Conditions for the simulations were 300 K and constant V for 5 ps. The PKA energy was varied from 4.25 to 300 eV and directed in the $\langle 1\,0\,0\rangle$, $\langle 1\,1\,0\rangle$, $\langle 1\,1\,1\rangle$, and $\langle 1\,2\,1\rangle$ directions. Four trajectories were run for each direction. The size of the simulation cell was varied from 256 to 2048 atoms, depending on the PKA energy. Periodic boundary conditions were assigned in all three Cartesian directions. A Nordsieck integrator [13] with a constant, 1 fs time-step was used throughout.

Initial conditions were selected by repeatedly equilibrating the undamaged lattice at the desired temperature and volume, with a Nosé–Hoover-drag thermostat activated with a 0.1 ps time constant [14]. At the start of a new cascade trajectory, new velocities were assigned to all atoms but the PKA. During a cascade trajectory, atoms other than the PKA were mildly thermostatted using the Nosé–Hoover-drag thermostat with a 10 ps time constant. The thermostatting was intended to mimic the thermal conduction of the electronic degrees of freedom, even though no quantitative basis was actually used in choosing the 10 ps time constant.

After a trajectory was run, the final configuration was subjected to a quenching process using a conjugate-gradient method. The quenching process was performed until the dot-products of the energy-gradients with the forces were reduced to 1×10^{-5} $(\mathrm{eV/nm})^2$ or less in absolute value. This was done to eliminate very short-lived defects without having to perform long annealing runs. Quenching made subsequent identification of defects more definitive.

4.2. Point-defect production

The results of at least four trajectories for each set of initial PKA energy and direction are reported here. First, we show a typical damage region as a result of the cascade. Besides the rhombohedral distortion of the MEAM model of δ-Pu, Fig. 4 also shows a residual interstitial defect and a vacancy left by the PKA cascade. The interstitial point defect is almost exclusively a structure that is split along one of the principle fcc axis directions. Analogous split interstitial defect clusters are also found in other fcc metals [15–17]. However, the bond distance for the Pu split interstitial is ≈0.25 nm, which is comparable to the shortest bonds in α-Pu. This short split-interstitial bond length is another manifestation of the thermodynamic proximity of the α-phase in the material. Without the lattice distortions (and therefore without the α-phase in the model), the radiation damage response of Pu would be similar to that of Pb with respect to its radiation damage response. The production of Frenkel pairs relative to the KP model is shown in Fig. 5. Each point for a given direction and projectile energy represents the average defect production for four trajectories. The average over the four directions sampled here is a weighted average for the damage production in each direction. Based on an ideal fcc unit cell, the $\langle 1\,0\,0\rangle$, $\langle 1\,1\,0\rangle$, $\langle 1\,1\,1\rangle$, and $\langle 1\,2\,1\rangle$ directions were weighted by 0.3, 0.3, 0.1, and 0.3, respectively.

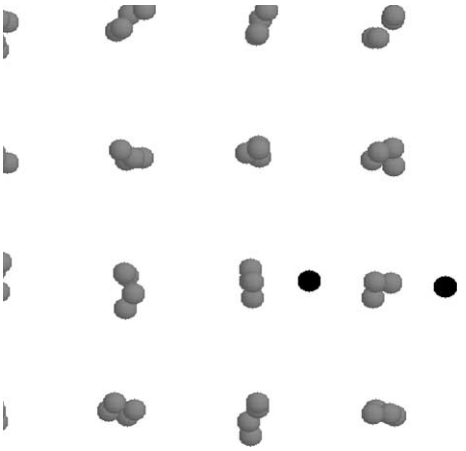

Fig. 4. Representative portion of a simulation cell of volume-stabilized Pu modeled with the MEAM potential of Ref. [3]. All the atoms shown are Pu. Two of the atoms denoted by a darker color participate in a split interstitial defect. The bond distance in the split interstitial is ~0.25 nm, which is comparable to the shortest bond lengths in α-Pu. During migration events the defect atoms exchange with neighboring atoms.

Based on these results, the minimum displacement threshold energy for fcc Pu at 300 K and constant V is estimated to be approximately 10 eV in the $\langle 1\,0\,0\rangle$ direction, i.e. the projectile energy at which each trajectory produces, on average, one Frenkel pair. The line in Fig. 5 represents the KP model [4,5] with 10 eV assigned to the minimum displacement threshold energy. Electronic losses are neglected in our simulations. The damage energy (upper axis in Fig. 5), which accounts for electronic losses, is estimated from Linhard, Scharff, and Schiott [4,18]. It is included here to show that neglecting electronic losses is not a serious concern in determining the minimum displacement threshold energy in δ-Pu metal.

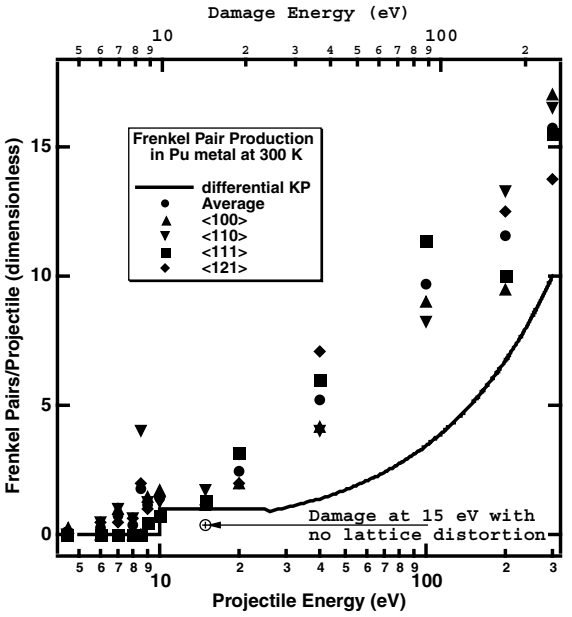

Fig. 5. Defect production after 5 ps at various projectile energies. The production levels are compared to the empirical KP model [4–6], which is concerned with defect production after a much longer annealing period. The point marked by the symbol $\oplus$ represents the defect production at 15 eV PKA energy when the parameter $t^{(3)}$ is set to zero in the MEAM potential. (See Table 1.) This makes the system behave much more like a normal fcc metal.

Table 2 compares the minimum displacement threshold energy for distorted δ-Pu with relatively well-characterized fcc metals. The distorted δ-Pu value comes closest to the lower experimental values of Pb. The present MD/MEAM value contrasts markedly with the value predicted by a correlation between displacement threshold energy and sublimation enthalpy [19]. The value for Pu predicted in that model is 33 eV. Another comparison is possible by forcing MEAM Pu to have the ideal fcc structure. This can be accomplished quite easily by setting $t^{(3)}$ in Eq. (3) to zero. In this case, the minimum displacement threshold energy is increased to approximately 16 eV, whereas Pb has a minimum displacement threshold energy of approximately 15 eV.

As an alternative, one could require the MD cascade Frenkel pair concentrations to agree with the KP model. In this case, one would predict an E_d of 6 eV. At the lower PKA energies considered here, the effective temperature within the cascade apparently does not permit as much annealing as one would expect based on the KP model. During the annealing phase of the cascade (after about 2 ps here), the recovery of the lattice is observably sluggish compared to recovery in other fcc metals. The complex nature of the potential inserts shallow local minima that frustrate the recovery process. In other words, the high Frenkel pair concentration at low cascade energies appears to be an effect of the multiple phases available to Pu metal as the cascade core cycles through its range of temperatures. Consequently we prefer the 10 eV value for E_d.

4.3. Point-defect migration: Split interstitial and monovacancy migration

Split interstitials that orient themselves along a principle crystallographic axis are common in fcc metals. The same seems to hold true for interstitials in the present model of δ-Pu metal. In the formation of a Frenkel pair, it appears energetically preferable for two atoms to straddle a lattice site, rather than having one at the lattice site and the other at the octahedral site of the fcc lattice. Also, in general, split interstitials migrate with very low activation energies, typically on the order of 0.05 eV. Again, the same holds true for this model of δ-Pu metal. For this reason, direct molecular dynamics simulations of interstitial diffusion could be carried out with the same boundary conditions and thermostatting as in the cascade simulations. Since no cascade events

Table 2
Comparison of minimum displacement threshold energies (E_d) for distorted δ-Pu and some fcc metals

Metal	Pu	Ag	Al	Au	Cu	Ni	Pt	Pb
Experiment E_d (eV)	33[a] 14[b]	25[e]	16[e]	36[e]	19[e]	23[e]	24[e]	12.5–15[f]
MEAM E_d (eV)	10[c] 16[d]			20.9[c]	17.7[c]	23.7[c]	24.1[c]	15[c]

The experimental values are for polycrystalline samples using electron beam irradiation, except for Pu.

[a] Ref. [19] value based on sublimation energies in fcc metals.

[b] Ref. [22] value based on melting temperature of metals.

[c] Present work.

[d] Present work, MEAM value with lattice distortion removed ($t^{(3)} = 0$ in Table 1).

[e] Ref. [4].

[f] Ref. [16].

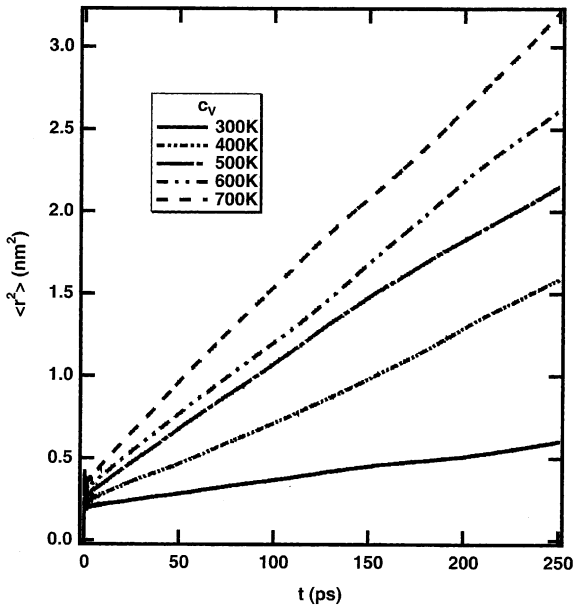

Fig. 6. Mean-square displacements of single dumbbell interstitial defects as functions of time for the 300–700 K temperature range at constant V. The slopes of the curves at later times (beyond 40 ps here), where the mean-square displacements become linear in time, are related to the diffusion constant for this defect through an Einstein relation. The predicted activation energy is a result of fitting an Arrhenius plot to the diffusion constants as a function of inverse temperature.

were active in this phase of the simulation, all atoms in the simulation were thermostatted. Also, for a single split interstitial, it was necessary to use only a small simulation cell. It was determined that the 256-atom cell with one interstitial added was sufficient for the diffusion constant determination. Fig. 6 shows the mean-square migration distances of $\langle 1\,0\,0\rangle$-oriented split interstitials versus time for a range of temperatures from 300 to 700 K at constant V. The slopes of the individual curves are related to the diffusion constant through an Einstein relation. An Arrhenius analysis of the plot as a function of temperature gives an activation energy of 0.056 eV at constant V, in-line with other fcc metals. The migration is three-dimensional. This fact is directly observable from the MD simulations. The mean-square migration distances versus time from 300 to 700 K at constant p were also calculated, but are not shown here. At the lower temperatures, the system contracts 15–20%. Consequently, the migration rates slow considerably compared to the constant-V cases. At the higher temperatures, the volume contractions cease and the migration rates become comparable to the constant-V cases. Because of the large volume contractions at lower T, it was concluded that the constant-V conditions were more representative of the behavior of the Ga-stabilized alloys of Pu.

The mono-vacancy migrates with an energy barrier of about 1 eV as determined by a transition-state theory (TST) approximation. A particular nearest-neighbor atom to a vacancy was chosen as the migration candidate. A line joining the vacancy site and the chosen atom was divided into 21 equally-spaced positions. At each position, the energy of the system was minimized subject to the constraints that the migrating atom stay within a plane perpendicular to the line and that the lattice as a whole not translate. As indicated in Fig. 7(a) and (b), the

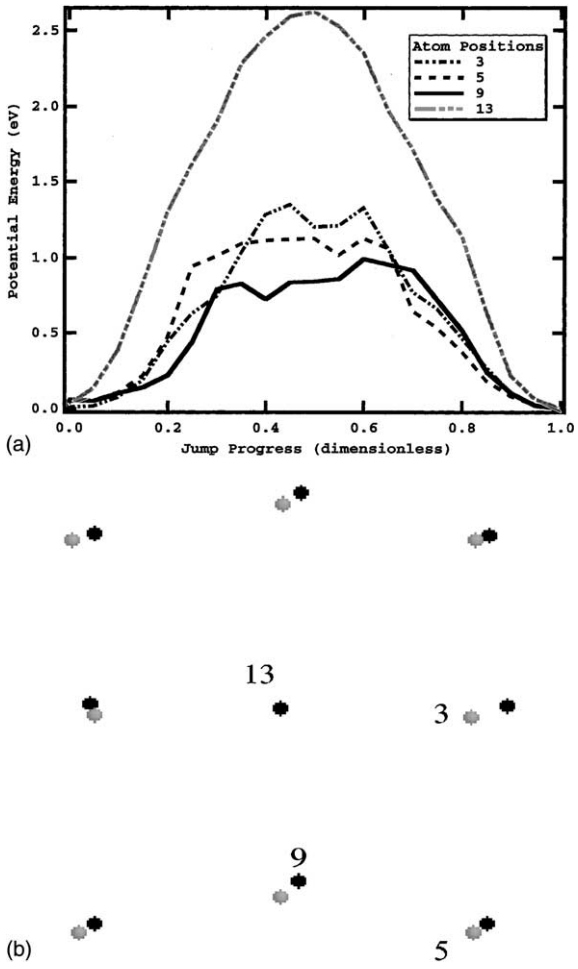

Fig. 7. Estimate of jump barrier for mono-vacancy diffusion. The curves in (a) are energy differences as various nearest-neighbor atoms attempt to fill the vacancy. The reference energy is for a cell with a mono-vacancy and all other atoms near their 'normal' distorted δ-Pu positions. The numbers in the legend correspond to the numbered atoms in (b). The jump path is a explained in the text. (b) Two (1 0 0) planes of distorted δ-Pu cell with a mono-vacancy. The gray circles are the plane with the mono-vacancy. The black circles are the plane behind the plane with the vacancy. The numbered atoms are some of the nearest-neighbors to the mono-vacancy.

jump directions were along nominally ⟨1 0 0⟩ and ⟨1 1 0⟩ directions. The line of atoms along the ⟨1 0 0⟩ directions were contracted substantially toward the ideal fcc lattice site location. For this reason, they were included as jump candidates. However, the optimal jump paths were still along the ⟨1 1 0⟩ directions. Even though there are just 2 inequivalent sites in distorted δ-Pu, the migration barriers showed much greater asymmetry. At this point, the asymmetry is not understood. Finally, the migration barriers for other neighbors not shown in Fig. 7(a) were estimated to be at least 0.5 eV higher than the minimum barrier.

The TST method is an indirect approach to determining the vacancy migration barrier because a jump path must be assumed, but it is convenient because of the high barrier. It is known that the migration path by this simple drag method might well be less than optimal, resulting in too high of a barrier estimate. As a check, direct MD simulations at 900 K for 10 ns were carried out, but resulted in no migration steps in this time interval. This time interval combined with a prefactor for the vacancy diffusion constant of 5×10^{8} m^2/s bounds the activation energy to 0.84 eV or more. More investigation is required before reaching a more definite conclusion on mono-vacancy migration barriers.

The sum of the vacancy migration barrier and the vacancy formation energy is approximately equal to the activation barrier for self-diffusion. The activation barrier for self-diffusion in Ga-stabilized Pu alloy has been reported to be between 0.8 and 1.5 eV [20–26], depending on the technique. Some of the techniques yielding larger self-diffusion barriers undoubtedly include the defect formation energy as well. Assuming this to be the case, these values imply a vacancy formation energy between 0.5 and 0.66 eV. From simple total energy calculations on the distorted δ-Pu lattice and the same lattice with a mono-vacancy, one finds 0.48 eV for the vacancy formation energy at 900 K. The 1.0 eV migration barrier and the 0.5 eV formation energy are close to the values for gold (Au) [25]. Furthermore, Timofeeva [26] finds a value of (1.1 ± 0.3) eV for the migration barrier from isothermal annealing experiments on Ga-stabilized δ-Pu. The ages and detailed compositions of the samples are not known. Fluss and coworkers [27] estimated a stage-III recovery temperature of 190 K from proton-radiation/isochronal annealing experiments on Ga-stabilized δ-Pu. This implies a vacancy migration barrier of (0.7 ± 0.1) eV. This vacancy migration energy is somewhat smaller than the one that we estimate. Earlier experiments on the resistivity of 4 at.% aluminum-stabilized Pu observes a stage-III recovery temperature of 164 K [28]. It is worth noting that all estimates rest on assumptions about the vibrational frequency associated with the migration path; the structural similarity of the atoms in the immediate vicinity of the vacancy in the experimental samples and the MEAM model; and the absence of effects on the migration mechanism from He, Ga, extended defects, and impurities in the samples. Despite the fact that we are mixing experimental values (1.5 eV) and modeling numbers, the picture for mono-vacancy migration and formation appears to be consistent. In summary, from the above analysis, distorted δ-Pu behaves more like Pb with respect to damage threshold, but more like Au with respect to point-defect transport.

Finally, the energy differences between the distorted δ-Pu lattice and the damaged lattices were calculated. From this information, two average defect-formation energies are estimated, one from the full range of defect energies and the other from only the lowest energy defects of each size. Fig. 8 shows the average energy change as a function of defect concentration for low concentrations, but extrapolated well beyond the concentration range from which the defect formation energy was deduced. If all of the defects are assumed to be a mono-vacancy or a single interstitial, one can estimate a configurational entropy contribution as a function of the defect concentration, and evaluate the change in free energy due to defects. One can see that at defect concentrations below 5%, the enthalpic change is too small

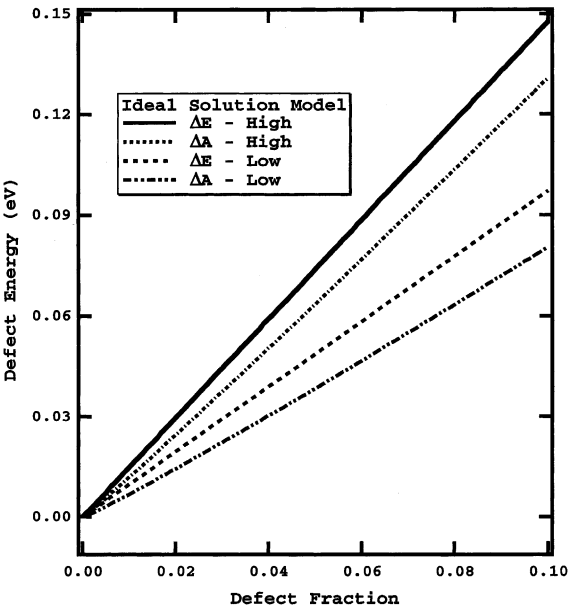

Fig. 8. Defect energy as a function of defect mole fraction. Energy per defect is calculated from an average over trajectories in these simulations at 300 K and constant V, i.e. for each PKA energy, each PKA direction, and sampling each of these initial conditions four times. 'ΔE' indicates an internal energy and 'ΔA' indicates a Helmholtz energy. The entropic contribution is strictly configurational. The 'High' model averages over all defects and the 'Low model only includes the lower-energy defects in the fits to the internal energies.

to induce phase transformations in an alloy such as Ga-stabilized Pu. However, fairly low defect concentrations may effect the positions of phase boundaries in the temperature–concentration phase diagram of Ga-stabilized Pu alloys.

5. Summary and conclusion

In summary, we find that for fcc Pu, at 300 K and constant V, the minimum displacement threshold energy is approximately 10 eV. This is lower than for lead, for instance, which has a minimum displacement threshold energy of 12.5–15 eV. The defect production appears much less anisotropic compared to other fcc metals such as Au and Pb. The cause of both the low minimum displacement threshold energy and the low anisotropy might be either the distortions in the fcc lattice or the presence of the lower-energy monoclinic phase or both. The symmetry of the rhombohedral distortions appears to be coincident with the $\langle 1\,1\,0\rangle$ orientations of the migration paths of point defects. The predominant point defect is a split interstitial oriented along the principle axes of the fcc crystal with a migration energy barrier of 0.056 eV. The migration is three-dimensional. Both of these facts were determined by direct MD simulations. The mono-vacancy migrates with a migration barrier of about 1.0 eV as determined by a TST approximation. The jump path prefers to be along a nominally $\langle 1\,1\,0\rangle$-type axis. The migration barriers for the various neighbors of the mono-vacancy are estimated to be as much as 0.5 eV higher. Direct simulations at 900 K for 10 ns resulted in no migration of the mono-vacancy. Volume stabilized δ-Pu behaves more like Pb with respect to damage threshold, but more like Au with respect to point-defect transport.

Acknowledgements

The aid of Albert Hung, MIT Department of Materials Science and Engineering, in calculating the MEAM displacement threshold energies in Table 2 is gratefully acknowledged. Those calculations were performed was part of a Los Alamos National Laboratory/MIT student exchange program. This work was performed under the auspices of the US Department of Energy by the Los Alamos National Laboratory under contract W-7405-ENG-36 with the University of California.

References

[1] M.S. Daw, M.I. Baskes, Phys. Rev. Lett. 50 (1983) 1285; M.S. Daw, M.I. Baskes, Phys. Rev. B 29 (1984) 6443.
[2] M.I. Baskes, Phys. Rev. Lett. 59 (1987) 2666; M.I. Baskes, Phys. Rev. B 46 (1992) 2727.
[3] M.I. Baskes, Phys. Rev. B 62 (2000) 15532.
[4] R.S. Averbach, T. Diaz de la Rubia, Solid State Phys. 51 (1998) 281.
[5] G.H. Pease, R.S. Pease, Rep. Prog. Phys. 18 (1955) 1; P. Sigmund, Radiat. Eff. 1 (1969) 15; P. Sigmund, Appl. Phys. Lett. 14 (1969) 114.
[6] M.J. Norgett, M.T. Robinson, I.M. Torrens, Nucl. Eng. Des. 33 (1975) 50.
[7] A. Goldberg, R.L. Rose, D.K. Matlock, Nuclear Metal. 17 (1970) 1056.
[8] A.C. Lawson, B. Martinez, J.A. Roberts, B.I. Bennett, J.W. Richardson, Philos. Mag. B 80 (2000) 53.
[9] A C. Lawson, J.A. Roberts, B. Martinez, J.W. Richardson, INVAR effect in Pu–Ga Alloys, Los Alamos National Laboratory report, LAUR-2002-4523.
[10] O.J. Wick, in: Plutonium Handbook: A Guide to the Technology, vols. I&II, The American Nuclear Society, 1980.
[11] H.M. Ledbetter, R.L. Moment, Acta Metall. 24 (1976) 891.
[12] R.B. Roof, in: D.K. Smith, C. Barrett, D.E. Leyden, P.K. Predecki (Eds.), Compression and Compressibility Studies of Plutonium and a Plutonium–Gallium Alloy, Plenum.
[13] J.R. Beeler, Radiation Effects Computer Experiments, North-Holland, 1982, p. 100.
[14] W.G. Hoover, Phys. Rev. B 31 (1985) 1695; S. Nosé, Prog. Theor. Phys. Suppl. 103 (1991) 1.
[15] H.-F. Deng, D.J. Bacon, Phys. Rev. B 48 (1993) 10022.
[16] T. Diaz de la Rubia, N. Soneda, M.J. Caturla, E. Alonso, J. Nucl. Mater. 251 (1997) 13.
[17] D.J. Bacon, F. Gao, Yu.N. Osetsky, J. Nucl. Mater. 276 (2000) 1.
[18] J. Linhard, M. Scharff, H.E. Schiott, Mater. Fys. Med. Vid Selsk 33 (1963) 14.
[19] M.F. Stevens, T.G. Zocco, R.C. Albers, J.D. Becker, K.C. Walter, B. Cort, D.L. Paisley, M.A. Nastasi, Final Report: Fundamental and Applied Studies of Helium Ingrowth and Aging in Plutonium, LA-UR-98-2606, 1998.
[20] R.D. Nelson, Plutonium 1965, Chapman and Hall, 1964, p. 639.
[21] R.E. Tate, E.M. Cramer, Trans. Metall. Soc.-AIME 230 (1964) 639.
[22] W.Z. Wade, J. Nucl. Mater. 38 (1971) 292; W.Z. Wade, D.W. Short, J.C. Walden, J.W. Magana, Metall. Trans. A 9A (1978) 965.
[23] D. Calais, J.P. Zanghi, J. Nucl. Mater. 39 (1971) 350.
[24] H. Schroeder, W. Schilling, Radiat. Eff. 30 (1976) 243; D.N. Borton, thesis, Rensselaer Polytechnic Institute, Troy, NY, 1973.
[25] T. Diaz de la Rubia, M.J. Caturla, E. Alonso, M.J. Fluss, J.M. Perlado, J. Comp.-Aided, Mater. Des. 5 (1998) 243.
[26] L.F. Timofeeva, in: K.K.S. Pillay, K.C. Kim (Eds.), International Conference on Plutonium-Future – The Science: Topical Conference on Plutonium and Actinides, AIP Conference Transactions, 2000, p. 11.
[27] B.D. Wirth, A.J. Schwartz, M.J. Fluss, M.J. Caturla, M.A. Wall, W.G. Wolfer, MRS Bull. 26 (2001) 679.
[28] R.O. Elliott, C.E. Olsen, in: G.J. Dienes (Ed.), Studies Radiat. Eff. Series A, Phys. Chem., vol. 1, Gordon and Breach, 1966, p. 1.